World Electric Vehicle Journal

Article

Direct Power Control of Vienna Rectifier Based on Fractional Order Sliding Mode Control

Tao Wang, Shenhui Chen *, Xin Li, Jihui Zhang and Jinghao Ma

Mechanical Engineering, College of Mechanical and Equipment Engineering, New Campus, Hebei University of Engineering, Handan 056038, China; wangtao24@hebeu.edu.cn (T.W.); lixinppmn@gmail.com (X.L.); 15893620363@163.com (J.Z.); m2403184949@126.com (J.M.)

* Correspondence: hg702csh@163.com

Abstract: Taking a Vienna rectifier as the research object, the power mathematical model based on a switching function is established according to its working principle. A sliding mode variable structure control algorithm based on the reaching law is examined in order to address the issues of the slow response speed and inadequate anti-interference of classical PI control in the face of abrupt changes in the DC-side load. In response to the sluggish convergence rate and inadequate chattering suppression of classical integer order sliding mode control, a fractional order exponential reaching law sliding mode, direct power control approach with rapid convergence is developed. The fractional calculus is introduced into the sliding mode control, and the dynamic performance and convergence speed of the control system are improved by increasing the degree of freedom of the fractional calculus operator. The method of including a balance factor in the zero-sequence component is employed to address the issue of the midpoint potential equilibrium in the Vienna rectifier. Ultimately, the suggested control is evaluated against classical PI control through simulation analysis and experimental validation. The findings indicate that the proposed technique exhibits rapid convergence, reduced control duration, and enhanced robustness, hence augmenting its resistance to interference.

Keywords: Vienna rectifier; sliding mode control; equilibrium of midpoint potential; fractional order control; zero-sequence component

check for updates

Citation: Wang, T.; Chen, S.; Li, X.; Zhang, J.; Ma, J. Direct Power Control of Vienna Rectifier Based on Fractional Order Sliding Mode Control. *World Electr. Veh. J.* **2024**, *15*, 543. https://doi.org/10.3390/wevj15120543

Academic Editor: Michael Fowler

Received: 23 October 2024
Revised: 15 November 2024
Accepted: 20 November 2024
Published: 22 November 2024

1. Introduction

The significance of power electronics technology in the energy management and power transmission systems of electric vehicles has increased in tandem with the rising global energy demand and the rapid progression of electric vehicle technology. Rectifiers are a crucial element of the electric vehicle charging system and are vital for the AC/DC conversion process [1,2]. But existing rectifier technologies are limited by energy efficiency bottlenecks, a poor power factor, and harmonic pollution, which not only jeopardize the grid power quality but also make it difficult to achieve the high efficiency, safety, and stability requirements for EV charging systems [3,4].

The Vienna rectifier has become a central subject of investigation in power electronics owing to its unique three-level neutral point-clamped structure [5]. This three-level AC/DC converter offers advantages over traditional PWM (Pulse Width Modulation) rectifiers, including a reduced number of switches, a simpler topology, diminished voltage stress on power-switching devices, the elimination of dead time settings, and enhanced power density. This enables the fulfillment of the need for the rapid charging of electric vehicles while concurrently improving the system efficiency and power quality [6,7]. In recent years, the Vienna rectifier has been widely employed across various energy sectors, including electric vehicle charging stations, power exchange apparatus, aviation power supplies, and wind power generation systems.

Currently, the control technique of the Vienna rectifier is a significant focus of scholarly attention within the industry. The primary control objectives of the rectifier are as follows:

first, to rapidly align the output voltage of the DC side with the goal voltage value; second, to guarantee stable operation at a unit power factor; third, to uphold the balance of the neutral point potential [8,9]. For control objectives one and two, the prevalent control methods are PI (Proportional–Integral) control and sliding mode control. Among these, PI control was the earliest control system integrated with PWM, and its straightforward design and ease of implementation are its notable features. A PI controller can augment stability and enhance the dynamic performance of the system in diverse operating situations [10]. The introduction of phase lag in the high-frequency domain may result in a reduction in the system response speed and induce oscillation. Extended deviations may result in integrator saturation, thereby reducing control effectiveness. In instances of substantial disturbances or rapid load fluctuations, the performance of the PI controller may be less effective than that of more advanced control methods [11]. Yang et al. employed a hybrid control technique integrating PI feedforward intervention and repeated control to enhance the quality of the input current waveform; nevertheless, following a load disturbance, the duration required for the DC-side output voltage to revert to the goal value was comparatively prolonged [12]. Wang et al. introduced a double closed-loop PI control system that mitigates current zero-crossing distortion, enhancing the grid-side power factor; nevertheless, it neglects the issue of DC-side voltage overshoot during rapid load changes [13]. Song et al. suggested that the voltage outer loop employs a PI controller, while the current inner loop utilizes an enhanced hysteresis control method. Despite its simplicity, the variable switching frequency complicates the circuit parameter design [14]. He et al. implemented the vector control of the optimized current PI regulator to satisfy the stability performance criteria of the rectifier under varying input voltages and inductance conditions; however, they did not address the circuit's dynamic performance [15]. With the increasing prevalence of Vienna rectifiers, the contexts of their application have become increasingly diverse, accompanied by escalating dynamic and static requirements. The rectifier is a sophisticated system characterized by nonlinearity, significant time variability, and strong coupling. Achieving the necessary control effect using the typical double closed-loop PI control technique is challenging [16,17].

Numerous researchers and experts from both domestic and foreign institutions have studied the rectifier and its cascade system in great detail using modern control methodologies in order to overcome the problems with the current three-phase rectifier. Because of its quick response, insensitivity to changes in parameters and disturbances, ease of physical implementation, and absence of a need for online system identification, the sliding mode variable structure control is the most representative [18,19]. The control is essentially a unique form of nonlinear control, characterized by the discontinuity of its control mechanism. The difference between this control strategy and others is that the system's 'structure' is not fixed; instead, it can dynamically adjust according to the system's current state (including deviations and their derivatives), intentionally modifying itself to ensure the system adheres to a specified 'sliding mode' state trajectory [20]. The literature suggests using sliding mode control on a three-phase rectifier to regulate the DC-side output voltage [21]. Wang et al. proposed a nonlinear sliding mode variable control for the voltage outer loop, which is unaffected by parameter variations and is straightforward to implement [22]. Ma et al. employed a sliding mode proportional resonant composite control technique. The enhanced electric sliding mode variable structure was employed for voltage outer-loop control, enabling a rapid response to voltage fluctuations and enhancing the system's dynamic performance and durability [23]. Yang et al. developed an adaptive voltage outer-loop sliding mode control technique utilizing an RBF (Radial Basis Function) neural network, which substantially diminishes switching losses and improves the system's resistance to interference [24]. Despite the aforementioned advantages of sliding mode control, it is not devoid of shortcomings. When the system's trajectory intersects with the switching surface, its velocity is not infinite; rather, inertia causes the moving point to traverse the switching surface, resulting in jitter vibrations that superimpose on the ideal sliding mode surface. Consequently, the inherent discontinuous switching characteristics of sliding mode variable structure control induce jitter vibrations in the system [25].

Professor Gao Weibing devised a method for chattering eradication in China. This approach employs the exponential order reaching rule to guarantee the dynamic quality of the sliding mode convergence process and can mitigate the high-frequency jitter of the control signal. Nonetheless, the significant rate of the system motion point moving toward the switching surface will still induce chattering. This work offers a fractional order exponential reaching law by including a fractional order calculus operator in the exponential reaching law to successfully address these issues. Utilizing sliding mode variable derivatives of a non-integer order mitigates the jitter phenomenon during the convergence process while sustaining a high convergence speed throughout the entire duration. A comparative analysis with alternative methods substantiates the efficacy of the proposed control strategy [26,27].

The third control target, the midpoint potential balance, can be divided into the following three categories:

1. The influence on the midpoint potential is counterbalanced by varying the action time of positive and negative redundant small vectors;
2. The variation in the neutral point potential is directly incorporated into the closed-loop control and modified through feedback;
3. The zero-sequence component is incorporated into the modulation wave to mitigate the variation in the midpoint potential [28–30].

In this paper, based on the idea of injecting a zero-sequence component into the carrier modulation and adding a balance factor on the basis of the zero-sequence component, a sliding mode direct power control strategy based on a fractional exponential reaching law is proposed by improving the reaching law. The strategy comprehensively considers stabilizing the output voltage, maintaining the midpoint potential balance, and maintaining the unit power factor operation, and can meet the sliding mode accessibility, existence, and arrival time boundedness requirements. The control rate designed according to this strategy has good dynamic and static stability and robust performance.

The remainder of this article is structured as follows: The second portion presents the power mathematical model of the Vienna rectifier. The third section presents the design of the voltage outer-loop controller. The fourth portion presents the inner-loop direct power control approach. The final portion presents the neutral point potential balance technique with similar SVPWM (Space Vector Pulse Width Modulation) technology. The control approach suggested in this paper is employed for simulation and experimental validation in the sixth section. The seventh segment presents the conclusion.

2. Three-Phase Vienna Rectifier Power Mathematical Modeling

The main circuit topology of the three-phase Vienna rectifier is shown in Figure 1. e_a, e_b, e_c is a rectified three-phase AC power supply; i_a, i_b, i_c is the three-phase input current for the DC bus positive and negative currents, i_p, i_n; L_a, L_b, L_c and R_a, R_b, R_c are the AC-side filter inductors and resistors, respectively, and the sizes are L_s and R_s, respectively. In the center is a rectifier bridge consisting of three pairs of fast-recovery diodes; $S_{a,b,c}$ is the switching function, and the structure of each of the three pairs of bidirectional switches consists of two MOSFETs (Metal Oxide Semiconductor Field Effect Transistors) in opposite directions, as shown in Figure 1. C_p and C_n are for the DC side of the upper and lower filter capacitance. The two capacitance values are equal; their value is C. The DC bus voltages of v_{dc}, v_{cp} and $v_{cn}\left(v_{cp} = v_{cn}\right)$, are the voltages of the upper and lower filter capacitors on the DC side, respectively; R_L is the output resistive load.

The Vienna rectifier is a current-driven power factor correction device. Its topology is a three-level circuit. The voltage at both ends of the power switch tube is determined by the state of the switch tube and the current direction of the current source side. Each phase bridge arm can be equivalent to a positive and negative boost circuit. Taking phase a as an example, if the input current is positive and the switch is turned off, the voltage at both ends of the switch is $v_{AN} = v_{cp}(v_{dc}/2)$; if the input current is negative and the switch is turned off, the voltage at both ends of the switch is $v_{AN} = v_{cn}(-v_{dc}/2)$. No matter whether the current is positive or negative, as long as the switch is turned on, the switch tube is clamped at the midpoint N of the DC side.

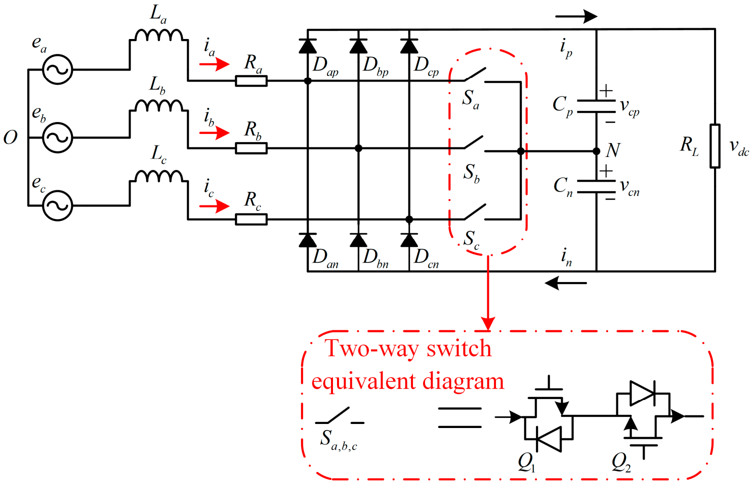

Figure 1. Topology of main circuit of Vienna rectifier.

Assuming that the grid voltage is in an ideal equilibrium state, the bidirectional power switch tube can be equivalent to a single-pole three-throw switch. The three-phase switching function S_K was introduced to represent the potential state of each phase switch, and S_K can be expressed as

$$S_K = \begin{cases} 1 & S_{ip} = 1, \quad S_{io} = 0, \quad S_{in} = 0 \\ 0 & S_{ip} = 1, \quad S_{io} = 0, \quad S_{in} = 0 \\ -1 & S_{ip} = 1, \quad S_{io} = 0, \quad S_{in} = 0 \end{cases} \begin{matrix} K = a, b, c \\ i = a, b, c \end{matrix} \tag{1}$$

Based on the three-phase grid voltage balance, the Vienna rectifier operates in a continuous current mode, and according to the above working process, the mathematical model can be obtained in the three-phase stationary coordinate system:

$$\begin{cases} L\frac{di_{a,b,c}}{dt} = e_{a,b,c} - R \cdot i_{a,b,c} - \left(v_{(a,b,c)N} + v_{NO}\right) \\ C\frac{dv_{Cp}}{dt} = S_{ap}i_a + S_{bp}i_b + S_{cp}i_c - \frac{v_{dc}}{R_L} \\ C\frac{dv_{Cn}}{dt} = S_{an}i_a + S_{bn}i_b + S_{cn}i_c - \frac{v_{dc}}{R_L} \end{cases} \tag{2}$$

where S_{ip} and $S_{in}(i = a, b, c)$ denote the switching functions with positive and negative current directions, respectively. Using the equal power transformation matrix, the mathematical model in the three-phase stationary coordinate system of Equation (2) was transformed to the α-β two-phase stationary coordinate system, and the corresponding transformation relationship is expressed as

$$\begin{bmatrix} x_\alpha \\ x_\beta \end{bmatrix} = \sqrt{\frac{2}{3}} \begin{bmatrix} 1 & -\frac{1}{2} & -\frac{1}{2} \\ 0 & \frac{\sqrt{3}}{2} & -\frac{\sqrt{3}}{2} \end{bmatrix} \begin{bmatrix} x_a \\ x_b \\ x_c \end{bmatrix} \tag{3}$$

The mathematical model in the α-β coordinate system obtained using the coordinate transformation formula is as follows:

$$\begin{cases} E_\alpha = R \cdot I_\alpha + L\frac{dI_\alpha}{dt} + V_\alpha \\ E_\beta = R \cdot I_\beta + L\frac{dI_\beta}{dt} + V_\beta \\ C\frac{dv_{cp}}{dt} = S_{\alpha p} i_\alpha + S_{\beta p} i_\beta - \frac{v_{dc}}{R_L} \\ C\frac{dv_{cn}}{dt} = -S_{\alpha n} i_\alpha - S_{\beta n} i_\beta - \frac{v_{dc}}{R_L} \end{cases} \tag{4}$$

In the equation, R_L is the load resistance, and L and R are the inductance and resistance of the input side, respectively. E_α, E_β, I_α, I_β, V_α, and V_β are the grid-side voltage, the grid-side current, and the voltage at both ends of the switch tube in the two-phase stationary α-β coordinate system, respectively.

The analysis of Equation (4) showed that the Vienna rectifier still had a certain coupling in the α-β coordinate system. The time-varying amount in the α-β coordinate system was converted into the direct flow in the d-q two-phase rotating coordinate system by Park transformation. The d-axis and q-axis were used to represent the active and reactive components of the rectifier system, respectively. The corresponding transformation relationship is expressed as

$$\begin{bmatrix} x_d \\ x_q \end{bmatrix} = \begin{bmatrix} \cos\omega t & \sin\omega t \\ -\sin\omega t & \cos\omega t \end{bmatrix} \begin{bmatrix} x_\alpha \\ x_\beta \end{bmatrix} \tag{5}$$

The mathematical model in the d-q coordinate system obtained using the coordinate transformation formula is

$$\begin{cases} L_s\frac{di_d}{dt} = -R_s i_d + \omega L_s i_q - \frac{1}{2} v_{dc} h_d + u_d \\ L_s\frac{di_q}{dt} = -R_s i_q - \omega L_s i_d - \frac{1}{2} v_{dc} h_q + u_q \\ C\frac{dv_{dc}}{dt} = h_d i_d + h_q i_q - 2\frac{v_{dc}}{R_L} \end{cases} \tag{6}$$

In the equation, $h_d = s_{dp} - s_{dn}$ and $h_q = s_{qp} - s_{qn}$, u_d, u_q, i_d, and i_q are the voltage and current components in the d-q coordinate system; ω is the AC angular frequency. The equivalent circuit model in the d-q coordinate system can be obtained using Equation (6), as shown in Figure 2.

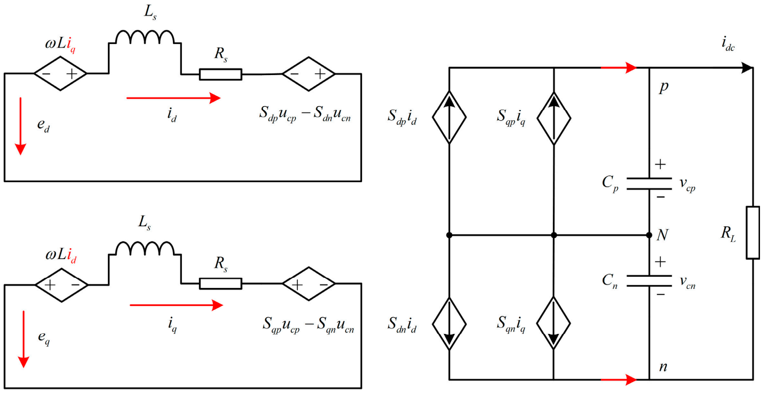

Figure 2. Equivalent circuit model in d-q coordinate system.

In the case of a balanced three-phase grid, based on the instantaneous power theory, the active and reactive power of the system can be expressed in terms of the voltage and current components in the d-q coordinate system:

$$\begin{matrix} P = u_d i_d + u_q i_q \\ Q = u_q i_d - u_d i_q \end{matrix} \tag{7}$$

In the d-q rotating coordinate system, by reasonably selecting the initial phase of the coordinate system, the initial phase angle of the d-axis was set to zero and coincided with the reference voltage vector of the grid. At this time, the q-axis component of the voltage was equal to zero, that is, $u_q = 0$. The calculation of Equation (7) can be obtained:

$$\begin{aligned} P &= u_d i_d \\ Q &= -u_d i_q \end{aligned} \tag{8}$$

Bringing Equation (8) into Equation (6) yielded a mathematical model of power control with P and Q as control variables:

$$\begin{cases} L_s \frac{dP}{dt} = -PR_s - \omega L_s Q - \frac{1}{2} v_{dc} h_d u_d + u_d^2 \\ L_s \frac{dQ}{dt} = -QR_s + \omega L_s p + \frac{1}{2} v_{dc} h_q u_q \\ u_d C \frac{dv_{dc}}{dt} = h_d P - h_q Q - 2 \frac{v_{dc}}{R_L} u_d \end{cases} \tag{9}$$

Utilizing P and Q as control variables, the subsequent control technique can directly modulate the active and reactive power inside the system, independent of conventional current or voltage transformation. This direct control method not only streamlines the control structure but also enhances the system's tracking capability to the power target. It responds more swiftly to abrupt shocks and decreases the control delay.

3. Design of Voltage Loop Controller

3.1. Design of Voltage Loop Fractional Order Sliding Mode Controller

A sliding mode variable structure is a kind of nonlinear structure control strategy. In the process of using a sliding mode variable structure control strategy to control the system, the control structure of the system is usually not fixed, but changes with the change in the running state of the whole system. For the control quantity of a discontinuous state, it is often judged by the S symbol of the sliding mode surface and changed according to the corresponding switching law. This control characteristic can force the system to move up and down with a small amplitude and high frequency along the prescribed state trajectory under certain characteristics, that is, the so-called sliding mode or 'sliding mode' motion. This sliding mode can be designed and has nothing to do with the parameters and disturbances of the system, that is, the sliding mode controller has good robustness to external disturbances and changes in internal parameters, so the application of the sliding mode variable structure control is very extensive.

The Vienna rectifier works under the unit power factor. When the system is stable, the output reactive power is 0, that is, $Q_{ref} = Q = 0$. According to the active power factor correction circuit of the Vienna rectifier, the calculation formula of the output active power can be obtained:

$$P = v_{dc} \cdot C \frac{d \frac{v_{dc}}{2}}{dt} + \frac{v_{dc}^2}{R_L} \tag{10}$$

where P is the output active power, R_L is the load resistance, and C is the value of the capacitance at the output.

In order to realize the tracking of DC voltage and keep it stable, as well as to improve the rapidity, accuracy, and robustness of the control system, the sliding mode variable structure control was selected as the outer loop of the voltage, and the state variable was chosen as the difference between the reference value and the actual value, and the sliding mode surface S was designed as follows:

$$S = \begin{bmatrix} s_1 \\ s_2 \end{bmatrix} = \begin{bmatrix} i_q^* - i_q \\ v_{dc}^* - v_{dc} \end{bmatrix} \tag{11}$$

where v_{dc}^* is the target voltage.

The derivation of Equation (11) was obtained:

$$\dot{S}_2 = -\frac{dv_{dc}}{dt} \tag{12}$$

The combination of Equations (10) and (12) can be obtained:

$$\dot{S}_2 = \frac{2v_{dc}}{R_L \cdot C} - \frac{2P}{v_{dc} \cdot C} \tag{13}$$

To weaken the jitter of the sliding mode variable structure, the exponential approach rate was selected, that is

$$\dot{S}_2 = -\varepsilon_0 \mathrm{sgn} S_2 - k_0 S_2 \; \varepsilon_0 > 0,\ k_0 > 0 \tag{14}$$

In the equation, k_0 and ε_0 are the convergence rate exponential coefficients and the rate at which the system converges to the switching surface, respectively; $\dot{S}_2 = -k_0 S_2$ is the exponential convergence term, and sgn is the sign function, that is

$$\mathrm{sgn}(S_2) = \begin{cases} 1 & x > 0 \\ 0 & x = 0 \\ -1 & x < 0 \end{cases} \tag{15}$$

The idea of the classical integer order sliding mode control strategy is to adjust the convergence law to make the system state quickly converge to the specified sliding mode surface, and perform the sliding mode motion along the sliding mode surface in accordance with the predetermined trajectory, so as to let the system error be minimized in a finite time. The exponential convergence law can provide better convergence, but its convergence speed may be limited by the setting of the ε_0 and k_0 values, which results in the system state not being able to reach the sliding mode surface to enter the sliding mode control phase in a finite amount of time and failing to meet the control requirements. Aiming to solve the problem of a slow convergence speed and poor chattering suppression effect in the integer order sliding mode control strategy, fractional order calculus was introduced into the classical sliding mode control algorithm, that is, a fractional order calculus operator was introduced into the exponential reaching law to form a fractional order sliding mode control strategy. The core idea of fractional calculus is to extend the classical calculus theory to the order other than the integer order, which has more general significance than the integer order calculus. The increased degree of freedom through the fractional calculus operator will improve the convergence speed of the system. At the same time, the non-integer order derivative of the sliding mode variable can reduce the chattering phenomenon in the reaching process. Moreover, the fractional order α can be adjusted to achieve the balance between the response speed and the control accuracy of the system, and the robustness of the system can be improved through its information memory characteristics.

The fractional exponential reaching law is

$$\dot{S}_2 = -\varepsilon_0 [D^\alpha \mathrm{sgn}(S_2)] - k_0 \cdot S_2 \tag{16}$$

In the equation, D^α is the calculus operator, $0 \le \alpha < 1$ is the fractional order, and $\alpha = 0$ is the exponential reaching law of the integer order. It can be seen that when the parameters of the sliding mode surface are determined, the fractional order sliding mode control can still adjust the dynamic performance of the system by adjusting the fractional order calculus operator α, while the integer order sliding mode control does not have the ability to adjust the performance so flexibly.

At the same time, the sign function $\mathrm{sgn}(S_2)$ is discontinuous near $S_2 = 0$, and the system will frequently switch positive and negative signs, resulting in high-frequency chattering. In order to reduce this phenomenon, the saturation function $sat(S_2)$ was used to replace the sharp switching of the sign function with a smooth transition when the value of S_2 is small. That is,

$$\dot{S}_2 = -\varepsilon_0 [D^\alpha sat(S_2)] - k_0 \cdot S_2 \tag{17}$$

The saturation function $sat(S_2)$ is

$$sat(S_2) = \begin{cases} \mathrm{sgn}(S_2) & |S_2| > \delta \\ \frac{S_2}{\delta} & |S_2| \leq \delta \end{cases} \tag{18}$$

In the equation, δ is the thickness of the boundary layer; when $|S_2| > \delta$, the existence of the fractional order ensures that the system converges to the sliding mode with a higher speed; when $|S_2| \leq \delta$, the sign function $\mathrm{sgn}(S_2)$ makes the transition to the sliding mode smoother by providing linear feedback within the boundary layer, ensuring fast convergence while weakening the jitter.

For the improved reaching law, when $S_2 = 0^+$ and $S_2 = 0^-$, the improved reaching law can be written as $\dot{S} \to 0$, that is, there is almost no chattering phenomenon when the system is in the critical steady state.

Equations (13) and (17) were combined to obtain the active power command value of the inner loop:

$$P_{ref} = \frac{\{\varepsilon_0[D^\alpha sat(S_2)] + k_0 S_2\} \cdot C v_{dc}}{2} + \frac{v_{dc}^2}{R_L} \tag{19}$$

According to the above analysis, the voltage outer-loop sliding mode variable structure control block diagram of the Vienna rectifier can be obtained from Equation (19), as shown in Figure 3.

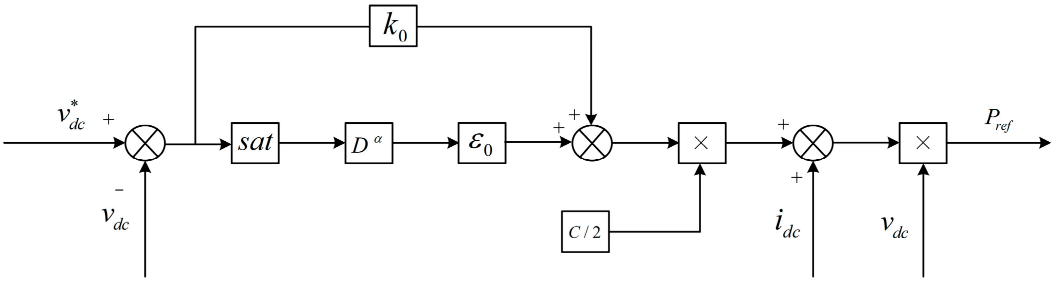

Figure 3. Sliding mode variable structure voltage outer-loop control block diagram.

3.2. Stability of the Sliding Mode Control Law

To verify the stability of the sliding membrane system, the positive definite function was constructed according to the Lyapunov stability theory:

$$V(S_2) = \frac{1}{2} S_2^2 \tag{20}$$

The derivation of this function was obtained:

$$\dot{V}(S_2) = S_2 \dot{S}_2 \tag{21}$$

The derivative of the sliding surface was represented by the form of the fractional exponential reaching law shown in Equation (17), and Equations (17) and (21) were combined to obtain

$$\dot{V}(S_2) = S_2[-\varepsilon_0 D^\alpha sat(S_2) - k_0 S_2] \tag{22}$$

Since $\varepsilon_0 > 0, k_0 > 0, \delta > 0$, Equation (22) can be discussed in two cases:
When $|S_2| > \delta$,

$$\dot{V}(S_2) = S_2 \dot{S}_2 = -k_0 S_2^2 - \varepsilon_0 S_2 D^\alpha \mathrm{sgn}(S_2) \leq 0 \tag{23}$$

When $|S_2| \leq \delta$,

$$\dot{V}(S_2) = S_2 S_2^2 = -k_0 S_2^2 - \frac{\varepsilon_0 S_2^2 D^\alpha}{\delta} \leq 0 \tag{24}$$

From the above analysis, $\dot{V}(S_2) = S_2\dot{S}_2 \leq 0$ can be obtained, and only when $S_2 = 0$, does $S_2\dot{S}_2 = 0$.

If the system is $S_2\dot{S}_2 \leq 0$, it is shown that the system is asymptotically stable in the sense of Lyapunov, and then the improved sliding mode reaching law can ensure the existence and accessibility of the sliding mode, that is, the system can reach the equilibrium point $S_2 = 0$ after adopting the improved sliding mode reaching law.

4. Inner-Loop Direct Power Control Strategy

The inner loop of the Vienna rectifier adopted the power control strategy and designed the PI regulator. The method was similar to the traditional three-phase rectifier, and the derivation process was no longer derived, and the derivation result was given directly. It can be seen from Equation (6) that due to the existence of ωL, the d-q axis current is coupled, resulting in the mutual coupling between the d-q axis power variables in Equation (9). In order to eliminate the influence of the coupling term, the independent DC variables were obtained so that the control of active and reactive components could be carried out independently. The power inner loop was decoupled by a feedforward process, and the decoupling control block diagram shown in Figure 4 was obtained.

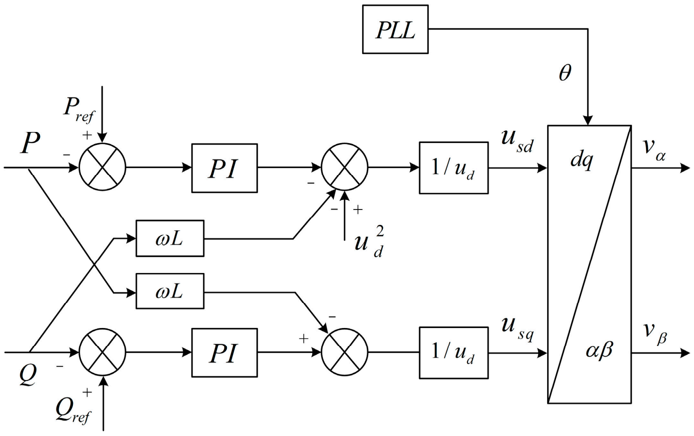

Figure 4. Power decoupling control block diagram.

After feedforward decoupling, the two coupling terms were eliminated and the system was transformed into a linear structure with which the design of the power inner-loop controller was carried out. To make the system operate at the unit power factor, suppose $Q_{ref} = 0$. The PI regulator in Figure 4 was used as the power inner-loop controller to obtain the mathematical model of the power inner-loop controller of the Vienna rectifier as follows:

$$\begin{cases} u_{sd} = -\left(k_p + \frac{k_i}{s}\right)\left(P_{ref} - P\right) - \omega LQ + u_d^2 \\ u_{sq} = \left(k_p + \frac{k_i}{s}\right)\left(Q_{ref} - Q\right) - \omega LP \end{cases} \tag{25}$$

In the equation, $u_{sd} = \frac{1}{2}v_{dc}u_d h_d$, $u_{sq} = \frac{1}{2}v_{dc}u_q h_q$, k_i is the integral gain of the PI regulator and k_p is the proportional gain.

According to the analysis of the above content, the dynamic performance of the system was greatly improved by using fractional order sliding mode control in the outer loop, and its output was the reference value of the active power in the inner loop. The PI control in the inner loop not only has a good control effect, but also simplifies the control system. The principle diagram of the control system of the Vienna rectifier is shown in Figure 5.

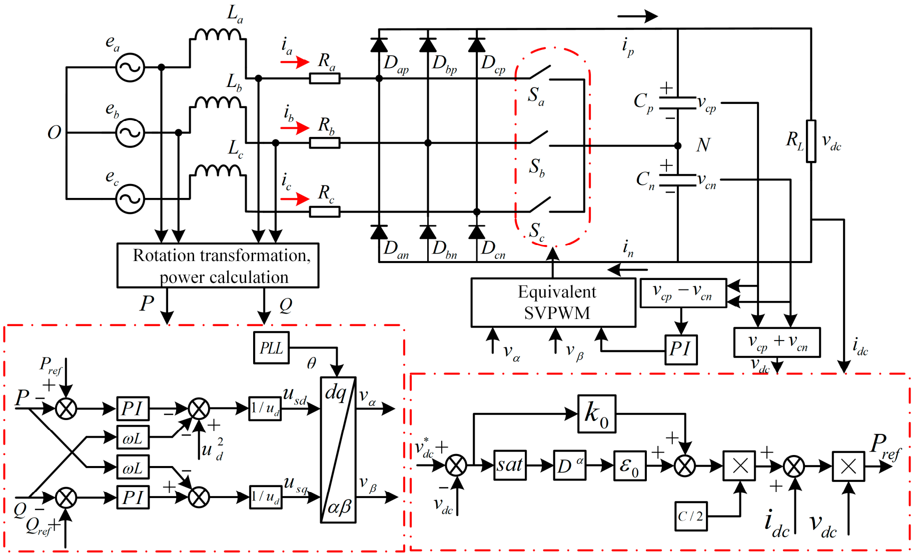

Figure 5. The control system block diagram of the Vienna rectifier.

5. Neutral Point Potential Balance Strategy Based on Equivalent SVPWM

Compared with the traditional three-level rectifier, the switch combination and zero vector distribution of the Vienna rectifier show different states. The zero vector is only $[0\ 0\ 0]$, while $[1\ 1\ 1]$ and $[-1\ \ -1\ \ -1]$ are two invalid states. The ideal way to adjust the midpoint potential balance is to use SVPWM, which can not only improve the load-side voltage utilization rate, but also reduce the switching loss. However, the calculation process is more complicated. In order to avoid re-judging the sector and calculating the vector action time, the method of injecting the zero-sequence component into the modulation wave was adopted. At the same time, a balance factor was added to the zero-sequence component to obtain a better midpoint potential balance ability, and the SVPWM effect was obtained. Figure 6 is the equivalent SVPWM principle block diagram.

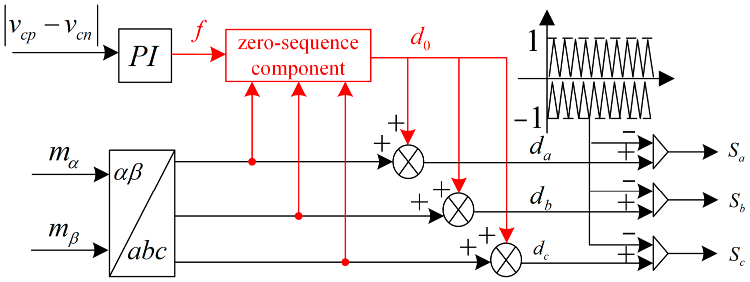

Figure 6. Carrier modulation algorithm based on equivalent SVPWM.

Since the division of the working sectors of the Vienna rectifier and the traditional three-level rectifier is different, it was necessary to re-divide the working sectors, as shown in Figure 7, with $-\pi/6 \sim \pi/6$ as the first large sector; a large sector was divided every 60 degrees, and then each large sector was divided into six small sectors.

The divided sectors are shown in Figure 7. Taking the first large sector as an example, V_{ref} was selected as the target vector of the small sector. At this time, the three-phase current is $i_a > 0, i_b < 0, i_c < 0$. The target vector V_{ref} adopts the principle of nearest vector synthesis, which is synthesized by V_2, $V_3(V_{3+}, V_{3-})$, and V_4. According to the principle of volt-second balance, the action time of each vector is:

$$V_4 T_4 + V_3 T_3 + V_2 T_2 = V_{ref} T_s \tag{26}$$

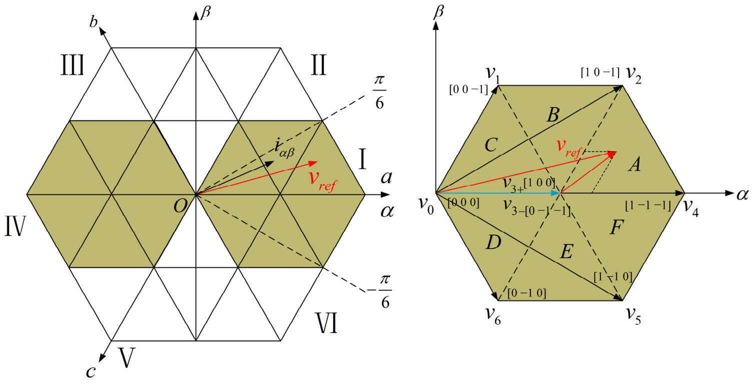

Figure 7. Vienna rectifier space vector plane diagram.

In the equation, T_4, T_3, and T_2 are the action time of the long vector V_4, short vector V_3, and medium vector V_2, respectively, and T_s is the sampling period. At the same time, T_4, T_3, T_2, and T_s satisfy the following relationship:

$$T_4 + T_3 + T_2 = T_s \tag{27}$$

We simplified Equation (26) by the real part and the imaginary part:

$$\begin{cases} |V_4|T_4 + \frac{\sqrt{3}}{2}|V_3|T_3 + |V_2|T_2 = |V_\alpha|T_s \\ \frac{1}{2}|V_2|T_2 = \left|V_\beta\right|T_s \end{cases} \tag{28}$$

According to $m = \sqrt{3}\left|V_{ref}\right|/|V_{dc}|$, the vectors in Equation (26) are normalized under the criterion of $|V_{dc}|$. The lengths of the long vector V_4, the middle vector V_2, and the short vector V_3 are $2V_{dc}/3$, $\sqrt{3}V_{dc}/3$, and $V_{dc}/3$, respectively, and are inverted to the three-phase stationary coordinate system using Clarke's inverse matrix, and the inversion matrix is shown below:

$$\begin{bmatrix} u_a \\ u_b \\ u_c \end{bmatrix} = \frac{1}{\sqrt{3}} \begin{bmatrix} 1 & 0 \\ -\frac{1}{2} & \frac{\sqrt{3}}{2} \\ -\frac{1}{2} & -\frac{\sqrt{3}}{2} \end{bmatrix} \begin{bmatrix} m_{ref\alpha} \\ m_{ref\beta} \end{bmatrix} \tag{29}$$

In the equation, u_a, u_b, and u_c are the variables of V_{ref} in the three-phase stationary coordinate system, and $m_{ref\alpha}$ and $m_{ref\beta}$ are the real and imaginary parts after transformation. Substituting Equations (26) and (27) into Equation (29), the action times of V_4, V_3 and V_2 are

$$\begin{cases} T_4 = (u_a - u_b - 1)T_s \\ T_3 = (2 - u_a + u_c)T_s \\ T_2 = (u_a - u_b - 1)T_s \end{cases} \tag{30}$$

The charging and discharging time of the upper and lower capacitors on the DC side was adjusted by allocating the action time of the small vector redundancy pair to achieve the midpoint potential balance, which satisfies the following relationship:

$$(1 - f)V_{3+} = fV_{3-} \tag{31}$$

In the equation, f is the time distribution coefficient of small vector redundancy to V_{3+} and V_{3-}, $0 < f < 1$; the value is controlled by the difference between the upper and lower capacitance voltages on the DC side through the pi regulator, in order to make the switching loss decrease and harmonic content decrease; the seven-segment time allocation mode is adopted; and there is a switching tube action for every change of vector; the start and end are selected as positive small vectors, and the middle is selected as a negative small vector. The modulation order with positive small vectors as initial vectors is as follows:

$$V_{3+}(1,0,0) - V_2(1,0,-1) - V_4(1,-1,-1) - V_{3-}(0,-1,-1) - V_4(1,-1,-1) - V_2(1,0,-1) - V_{3+}(1,0,0) \tag{32}$$

The operating times of the three switching tubes $S_{a,b,c}$ are derived from Equations (28) and (30)–(32):

$$\begin{cases} T_a = [u_a^* - u_c^* + f(u_c^* - u_a^*) + 2f - 1]T_s \\ T_b = \left[-u_b^* + u_c^* - f(u_c^* - u_a^*) - 2f + 1\right]T_s \\ T_c = [-f(u_c^* - u_a^*) - 2f + 1]T_s \end{cases} \tag{33}$$

Collating Equation (33) gives

$$\begin{cases} d_a = u_a^* + d_0 \\ d_b = -u_b^* - d_0 \\ d_c = -u_c^* - d_0 \\ d_0 = 2f - u_c^* + f(u_c^* - u_a^*) - 1 \end{cases} \tag{34}$$

The above formula is the zero-sequence component of V_{ref} located in the small sector of the first large sector A. When V_{ref} is located in other sectors, the zero-sequence component corresponding to each sector can be deduced according to the above process. In order to simplify the analysis and make it have a unified expression, the three-phase modulation wave was redefined as follows:

$$M_k = \begin{cases} u_k^* & u_k^* \geq 0 \\ u_k^* + 1 & u_k^* < 0 \end{cases} \quad k = a, b, c \tag{35}$$

Then, the injected zero-sequence component is as follows:

$$d_0 = f(1 - M_{\max} + M_{\min}) - M_{\min} \tag{36}$$

The injection of the zero-sequence component yielded an analogous SVPWM effect, facilitating the balancing of the midpoint potential.

6. Simulation and Experimental Verification

6.1. Analysis of Simulation Results

The simulation parameters in Table 1 (except the controller part) were used to verify the effectiveness of the control algorithm proposed in this paper.

Table 1. Simulation parameters.

Parameter	Numerical Value
Three-phase AC voltage effective value V_{rms}/V	220
Grid frequency f/Hz	50
Input inductance L/H	0.002
Input resistance R/Ω	0.05
DC reference voltage V_{dc}^*/V	600
Filter capacitor C/mF	3.2
Load resistance R/Ω	70
Switching frequency f_s/kHz	20

The proposed control strategy was compared with the classical PI control, as shown in Figure 8. Figure 8a,b are the DC-side voltage output waveforms of the classical PI control strategy and the proposed control strategy, respectively. Both strategies can maintain the stable DC-side voltage output at 600 V under steady-state conditions. It can be easily obtained from the data in the figure that the overshoot of the classical PI control is large; the voltage initially rises to about 650 V, the overshoot is 50 V, and there is still up-and-down oscillation in the process of stabilizing after the overshoot, and it takes about 80 ms to recover to stability. The initial value of the DC-side voltage of the proposed control strategy rises rapidly to 610 V, and then falls back and stabilizes at about 600 V, with an overshoot of only 10 V, and it takes only 40 ms to stabilize, and after stabilization, the ripple is very small, and the output voltage fluctuates within ±0.2 V, which indicates that the system can be well controlled near the target voltage in the steady state. Figure 8c,d are the voltage waveforms of the upper and lower capacitors on the DC side of the two control strategies, respectively. Under the classical PI control, the oscillation is relatively large, and the time required for complete stability is long. The proposed control algorithm has a small amplitude oscillation at the initial time, but it disappears quickly. The voltage fluctuation amplitude is small, which is always maintained within 0.5 V, and the system shows good dynamic performance. It can be concluded that the proposed control algorithm is superior to the classical PI control algorithm in terms of the dynamic response speed, overshoot control, and stability. Although the classical PI control algorithm is stable in a steady state, its initial response is slow, the overshoot and oscillation are large, and its performance is not as good as the proposed control strategy.

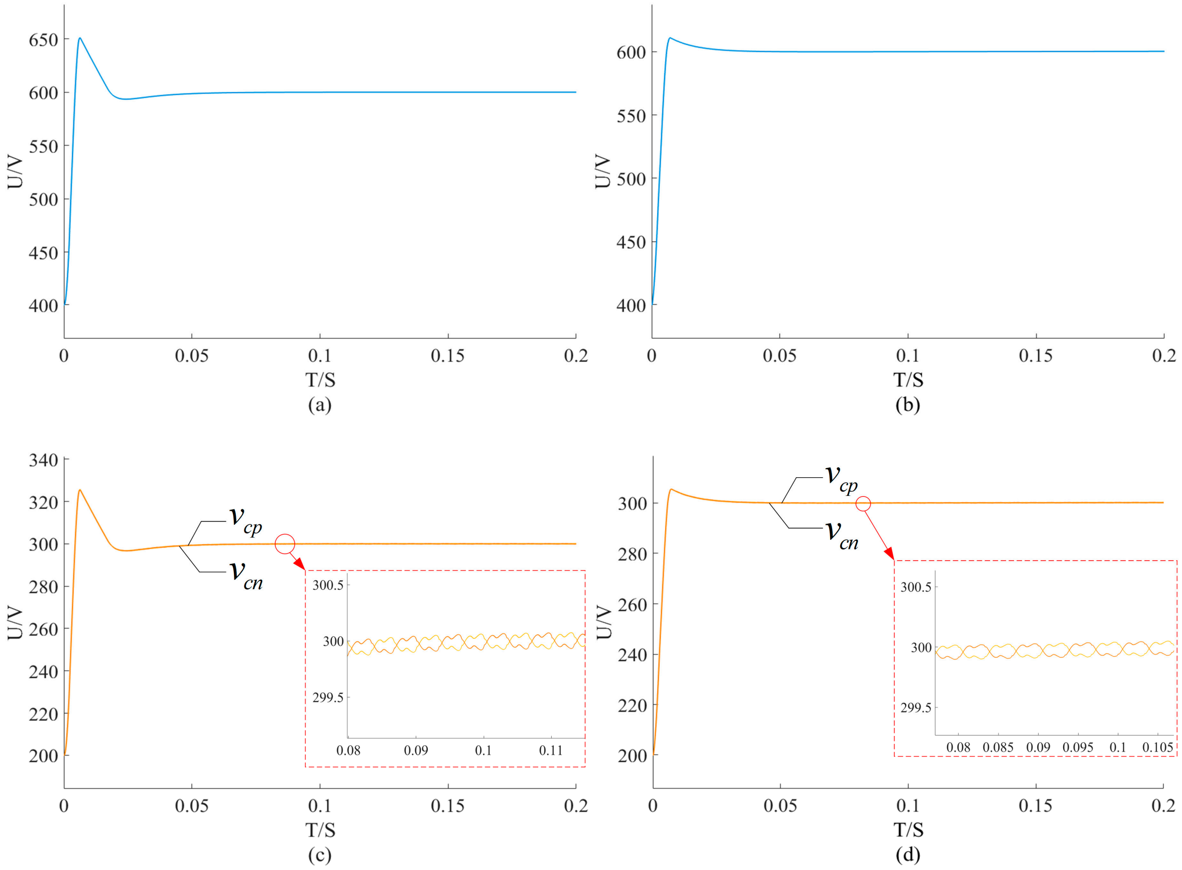

Figure 8. Voltage simulation waveforms of two control strategies. (**a**) The DC-side voltage waveform of classical PI control; (**b**) DC-side voltage waveform of fractional order sliding mode direct power control; (**c**) The upper and lower capacitor voltage waveform of classical PI control; (**d**) The upper and lower capacitor voltage waveform of fractional order sliding mode direct power control.

To compare the influence of the two control algorithms on the input current waveform, the simulation data of the grid-side current under the stable state of the two control methods was analyzed through Fourier analysis (FFT). From the beginning of 0.02 s, five cycles were sampled. From Figure 9, it can be concluded that the initial current of the classical PI control strategy fluctuates greatly, the oscillation duration is long, about 0.02 s, and the THD (Total Harmonic Distortion) in the fluctuation is more obvious; the THD = 2.29%. The current waveform of the proposed control strategy shows obvious smoothness. Although there is obvious oscillation at the beginning, it tends to become stable quickly in a short time (about 0.01 s), and the harmonic content is low; the THD = 0.81%. Compared with Figure 9e,f, it can be seen that after using the fractional order sliding mode direct power control algorithm, the THD value is reduced by 1.48%, the grid-side current quality is obviously improved, and the current waveform is sinusoidal. It is proved that the proposed control strategy is superior to the classical PI control in realizing the unit power factor, reducing the current harmonic content, and improving the grid-side current quality.

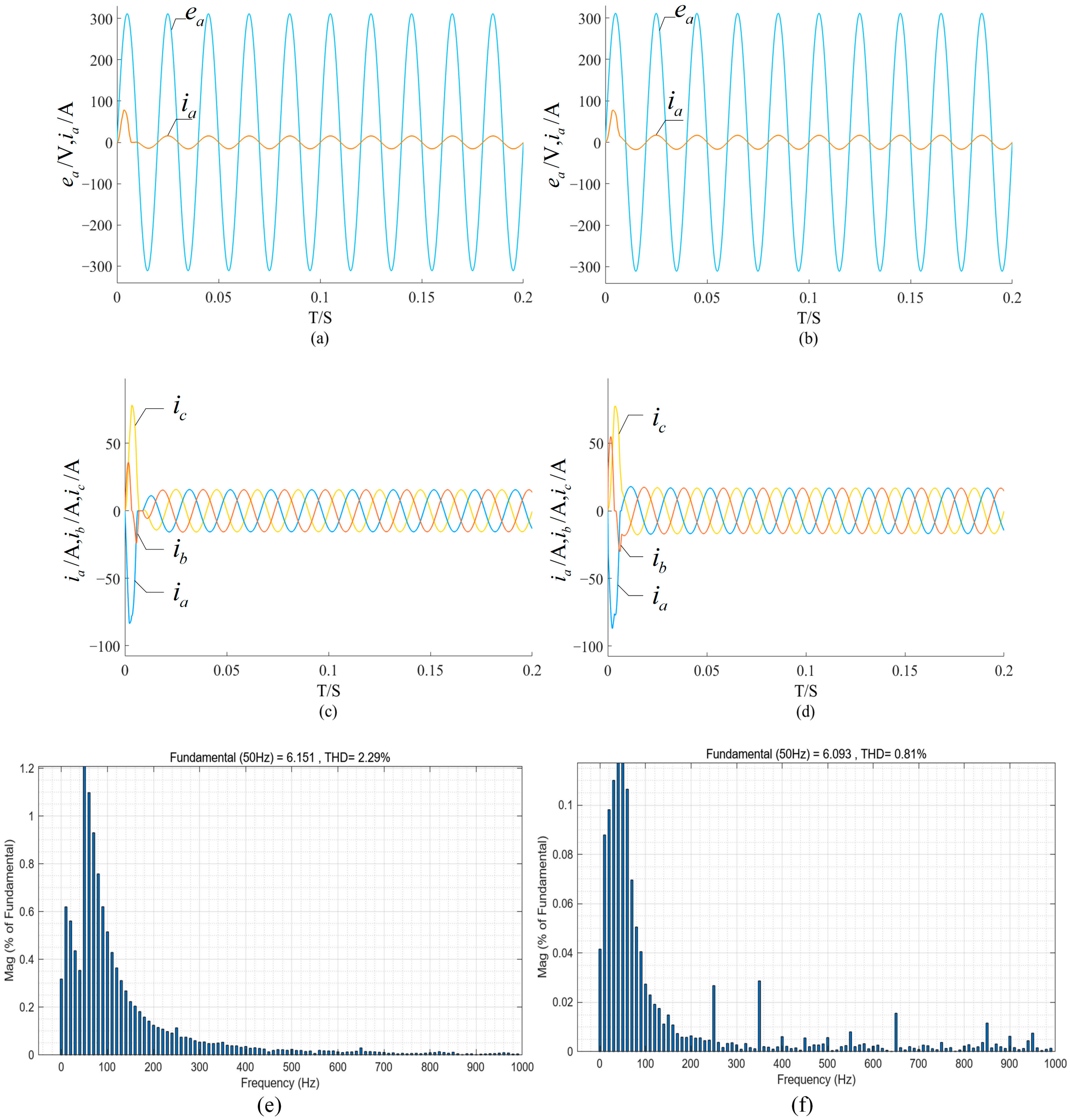

Figure 9. Simulation diagram of two control strategies of current and harmonics. (**a**) The A-phase current and voltage waveform of classical PI control; (**b**) A-phase current and voltage waveform of fractional order sliding mode direct power control; (**c**) Three-phase current waveform of classical PI control; (**d**) Three-phase current waveform diagram of fractional order sliding mode direct power control; (**e**) Harmonic content analysis diagram of classical PI control; (**f**) Harmonic content analysis diagram of fractional order sliding mode direct power control.

To verify the control performance of the classical PI control strategy and the proposed control strategy, the system was simulated and verified at a 0.08 s load mutation. The load resistance was 70 Ω; in order to make the load resistance value of the circuit change to an integer value of 60 Ω, a resistor with a resistance value of 420 Ω needed to be connected in parallel. The simulation waveform is shown in Figure 10. Figure 10a,c,e,g,i are the simulation waveforms under the classical PI control when the load mutation occurs, and Figure 10b,d,f,h,j are the simulation waveforms under the proposed control strategy. After the load changes abruptly, the two control strategies can finally maintain the DC-side voltage output of 600 V. The DC-side voltage of the classical PI control will drop to 594 V when the load changes suddenly, resulting in a fluctuation of about 6 V, and the fluctuation is more obvious. It takes 60 ms for the load to change abruptly to restore stability, and the dynamic response speed is slow. The proposed control strategy will reduce the DC-side voltage to 594 V when the load changes abruptly, and quickly stabilizes after a slight decrease. It will only produce a fluctuation of 4 V, and then quickly returns to the target voltage within 20 ms, and the midpoint potential balance can be quickly achieved. This verifies that the method of fractional order sliding mode direct power control in the outer loop can quickly force the operation trajectory of the system to move to the sliding mode surface and improve the response speed of the system. It can be seen that in the case of a sudden load change, the voltage recovery time of the proposed control strategy is very fast, and the classical PI control needs a longer time to eliminate the oscillation. The new control strategy shows a better dynamic response performance, which can better cope with sudden changes and maintain the stability of the system.

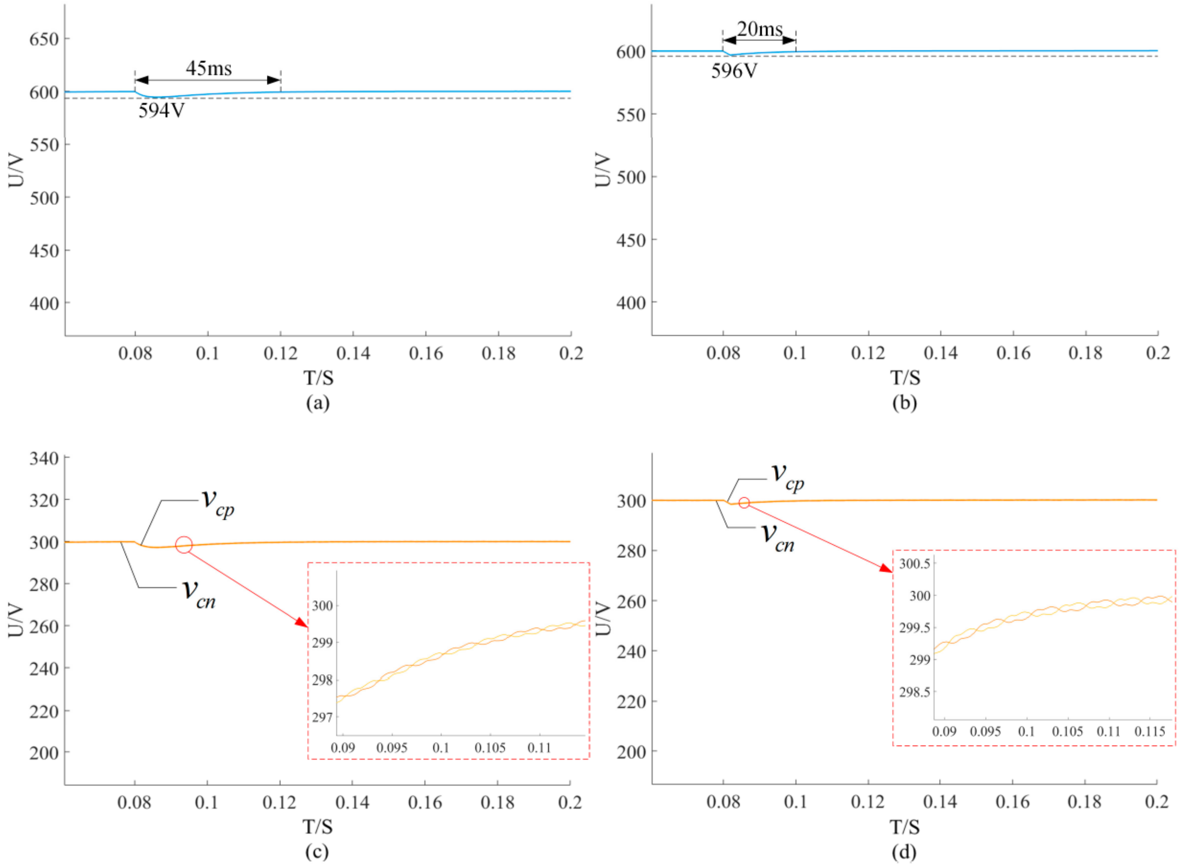

(a) (b)

(c) (d)

Figure 10. *Cont.*

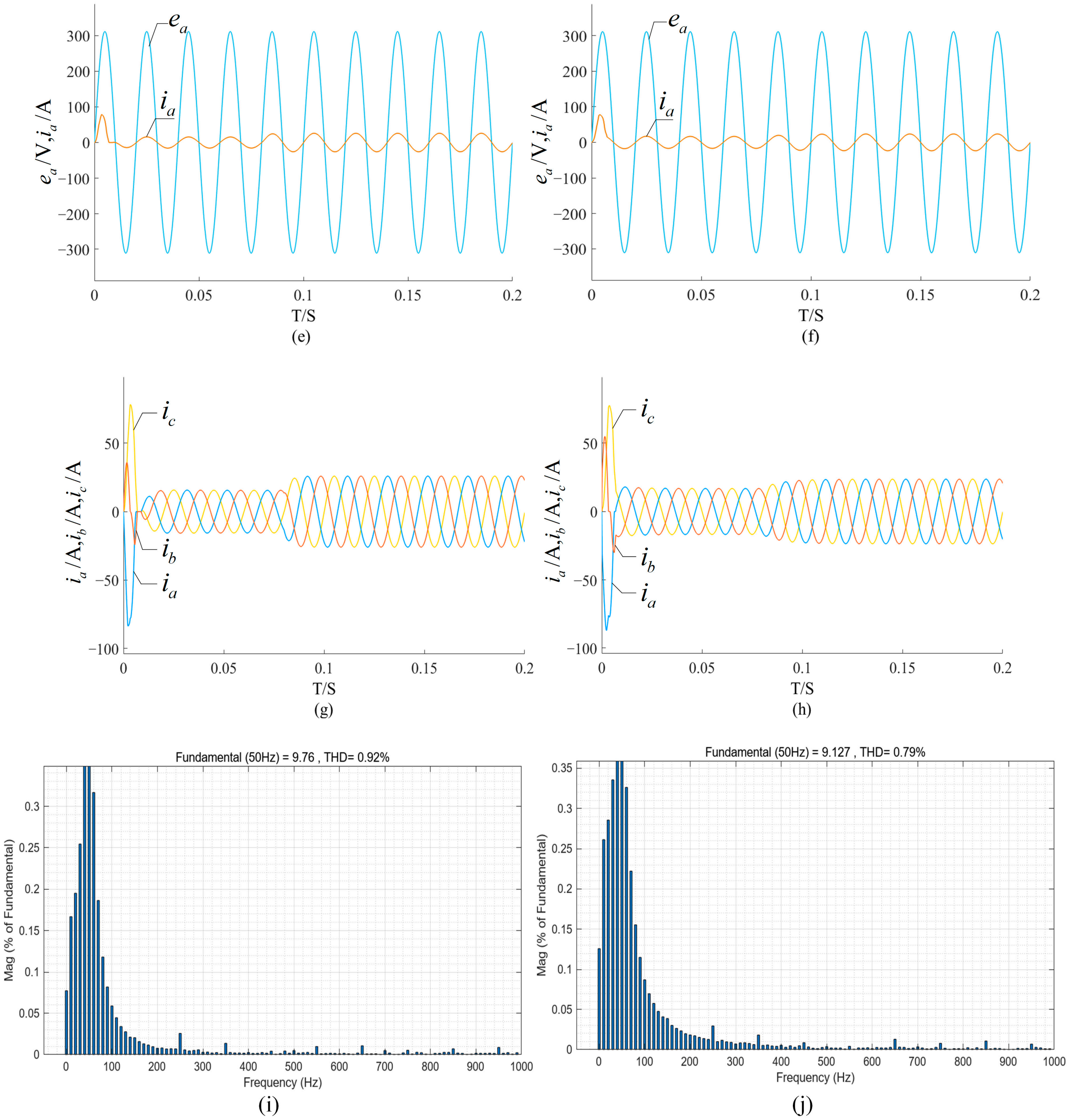

Figure 10. Simulated waveforms of the two control strategies during a sudden load change. (**a**) The DC-side voltage waveform of classical PI control under a sudden load change; (**b**) DC-side voltage waveform of fractional order sliding mode direct power control under a sudden load change; (**c**) The upper and lower capacitor voltage waveform of classical PI control under a load mutation; (**d**) Voltage waveform of upper and lower capacitors of fractional order sliding mode direct power control under a sudden load change; (**e**) The A-phase current and voltage waveform of classical PI control under a sudden load change; (**f**) Waveforms of A-phase current and voltage for fractional order sliding mode direct power control under a sudden load change; (**g**) Three-phase current waveform of classical PI control under a sudden load change; (**h**) Three-phase current waveform of fractional order sliding mode direct power control under a sudden load change. (**i**) The classical PI control THD value when the load changes suddenly; (**j**) The THD value of fractional order sliding mode direct power control when the load changes suddenly.

It can be seen from Figure 10e–j that when the load changes abruptly, the grid-side current under the classical PI control strategy cannot quickly track the voltage change and cannot be stabilized in time. The sinusoidal state of the grid-side current waveform is distorted and cannot resist the system disturbance well. The input current THD of the proposed control strategy is 0.79% after the sudden change in the load is stable, the current distortion is small, and the grid-side current is always sinusoidal, so that the system has better power quality and maintains system stability.

The performance of the output DC voltage is presented in Table 2. Table 2 illustrates that the DC-side voltage overshoot and adjustment time of the classical PI control technique are the most significant, and the grid-side current THD is also comparatively high before and after the load mutation. When the fractional order sliding mode control algorithm is used, the overshoot, rise time, adjustment time, and the THD of the grid-side current before and after the load mutation are further improved, and the anti-interference ability and dynamic performance of the system are improved.

Table 2. Comparison of control performance parameters.

Parameter	Classical PI Algorithm	New Algorithms
Overshoot/%	8.33	1.66
Rise time/s	0.006	0.006
Accommodation time/s	0.08	0.04
THD before load mutation/%	2.29	0.81
THD after load mutation/%	0.92	0.79
The fluctuation of the DC-side voltage when the load changes suddenly/V	6	4
The DC-side voltage's recovery stability time when the load changes suddenly/V	0.045	0.02

6.2. System Experimental Verification

In order to verify the effectiveness of the improved sliding mode reaching law control strategy proposed in this paper, the Vienna rectifier experimental platform shown in Figure 11 was built. The experimental parameters are shown in Table 1. The controller used Texas Instruments TMS320F2812DSP as the controller to perform real-time control. The digital signal processor could communicate with the host computer through the analog input and output channels of RL-LAB to achieve closed-loop control.

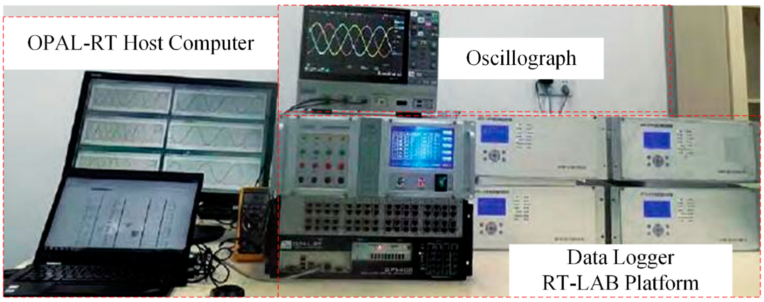

Figure 11. Vienna rectifier experimental platform.

The experimental waveforms are shown in Figure 12; through analysis, it can be seen that both control strategies can achieve stable control performance requirements. In load mutation experiments on the system, using the proposed control strategy, the speed of the upper and lower capacitor voltage tracking the specified value is improved a lot relative to the classical PI control strategy, and when the load changes, its output voltage can still be stabilized at the specified value after very small fluctuations, and the error of the midpoint potential does not change a lot, with very small fluctuations, and the stability has been optimized.

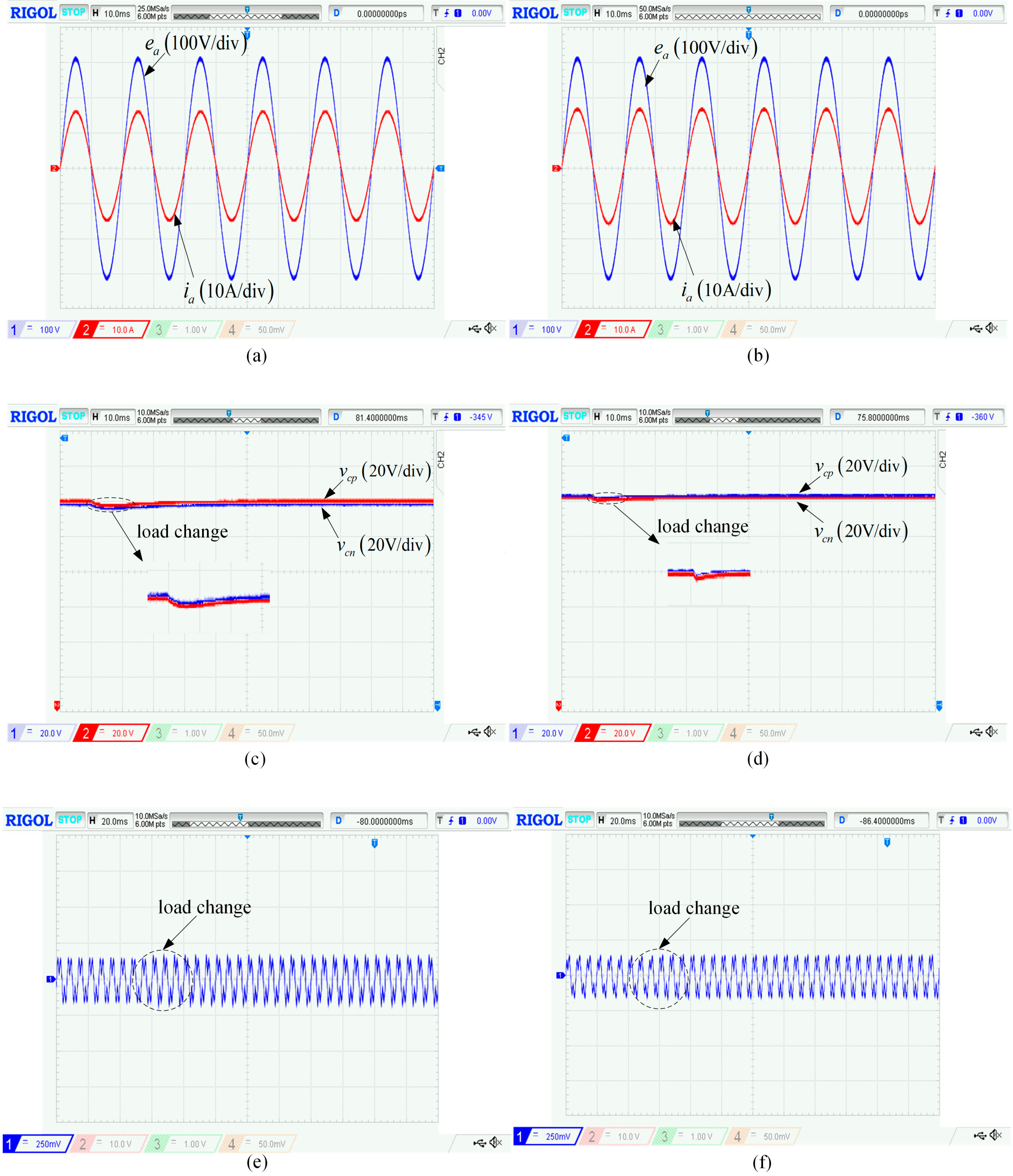

(a) (b) (c) (d) (e) (f)

Figure 12. Experimental waveforms of two control strategies. (**a**) The A-phase current and voltage experimental diagram of classical PI control; (**b**) Experimental diagram of A-phase current and voltage of fractional order sliding mode direct power control; (**c**) The upper and lower capacitor voltage experimental diagram of classical PI control; (**d**) Experimental diagram of upper and lower capacitor voltage of fractional order sliding mode direct power control; (**e**) The experimental diagram of the midpoint potential error of classical PI control; (**f**) Experimental diagram of the midpoint potential error of fractional order sliding mode direct power control.

7. Conclusions

This work proposes a fractional order sliding mode control approach for the voltage loop of a Vienna rectifier. In comparison to the classical PI control technique, the system's performance is markedly enhanced. Fractional order sliding mode control employs fractional order calculus operators to mitigate high-frequency jitter in the control signal, decrease the response time, and preserve stability during transient situations, thereby outperforming the linear response of classical PI control. The aforementioned simulation comparison and experimental findings demonstrate that the proposed control strategy effectively mitigates output voltage fluctuations on the DC side during the system initiation and load variations, resulting in a manageable and minimal ripple in the DC-side voltage. It facilitates expedited stability, reduced voltage fluctuations, and an enhanced load transient response, and bolsters the system's resistance to interference. Simultaneously, it may mitigate current harmonics on the grid side, ensure that the input current on the AC side is sinusoidal, and enhance the power quality. This paper's shortcoming is its failure to take into account the potential effects of extreme or irregular conditions on the system stability. Future studies will be carried out in the following areas.

1. The conventional sliding mode control algorithm has a chattering issue, which significantly affects the system's stability. Future studies will concentrate on the sophisticated sliding mode control algorithm to address the chattering issue associated with conventional sliding mode control and to improve the system's robustness in unpredictable situations;
2. In this paper, a control method involving the injection of zero-sequence components into the modulating waveform and the incorporation of a balance factor was employed for midpoint potential balancing. This necessitated an additional PI controller to fine-tune the balance factor. Future research will explore a hybrid modulation algorithm that integrates the midpoint potential with outer-loop sliding mode control, optimizing resource utilization while enhancing control performance.

Author Contributions: Conceptualization, T.W.; software, writing—original draft preparation, and writing—review and editing, S.C.; formal analysis, X.L.; investigation, J.Z.; validation, J.M. All authors have read and agreed to the published version of the manuscript.

Funding: This research received no external funding.

Data Availability Statement: The original contributions presented in the study are included in the article, further inquiries can be directed to the corresponding author.

Conflicts of Interest: The authors declare no conflicts of interest.

References

1. Kanakadhurga, D.; Prabaharan, N. Smart home energy management using demand response with uncertainty analysis of electric vehicle in the presence of renewable energy sources. *Appl. Energy* **2024**, *364*, 123062. [CrossRef]
2. Jiang, B.-H.; Hsu, C.-C.; Su, N.-W.; Lin, C.-C. A Review of Modern Electric Vehicle Innovations for Energy Transition. *Energies* **2024**, *17*, 2906. [CrossRef]
3. Fu, X.; Wang, H.; Guo, X.; Shi, C.; Jia, D.; Chen, C.; Guerrero, J.M. A Novel Circulating Current Suppression for Paralleled Current Source Converter Based on Virtual Impedance Concept. *Energies* **2022**, *15*, 1952. [CrossRef]
4. Huber, L.; Borojevic, D. Space vector modulated three-phase to three-phase matrix converter with input power factor correction. *IEEE Trans. Ind. Appl.* **1995**, *31*, 1234–1246. [CrossRef]
5. Kalaiarasi, N.; Fernandez, S.G.; Doss, M.A.N.; Vaishali, U.; Jayakumar, M.; Aridoss, V.; Nithyanandham, S. Analysis of Vienna rectifier. *AIP Conf. Proc.* **2024**, *3037*, 020056.
6. Cheng, H.; Zhao, Z.; Wang, C. A Novel Unidirectional Three-Phase Multilevel Rectifier Composed of Star-Connected Three Single-Phase Topology Based on Five-Level Flying Capacitor DC–DC Converter. *IEEE Trans. Ind. Electron.* **2022**, *70*, 5493–5503. [CrossRef]
7. Wang, X.; Kong, M. Transient characteristics and protection coordination strategy of hybrid AC/DC system based on modular multilevel converters under AC/DC transmission lines touching fault. *Energy Rep.* **2024**, *11*, 4213–4221. [CrossRef]
8. Zhu, T.; Du, G.; Deng, Z.; Lei, Y. Hybrid-paralleled power-factor-correction system for high-power equipment harmonic suppression. *J. Power Electron.* **2024**, *24*, 1450–1461. [CrossRef]
9. Tang, X.; Tang, Y.; Xu, Y. Suppression Strategy for Midpoint Potential Fluctuation of Three-Level Wind Power Converter. *IEEE Trans. Power Electron.* **2021**, *37*, 2583–2592. [CrossRef]
10. Shi, H.; Zhang, Z.; Han, J.; Li, J. Dynamic Performance Improvement of Wound Rotor Synchronous Starter/Generator System Based on PWM Rectifier. *IEEE Trans. Transp. Electrif.* **2023**, *9*, 4639–4649. [CrossRef]

11. Wang, C.; Wang, H.; Wang, Q. Circulating current suppression strategy of modular multilevel converter based on double PI controller. *Power Syst. Technol.* **2014**, *38*, 2905–2912.
12. Yang, D.; Yao, G.; Zhou, L. An Improved Control Method of 4-Wire Vienna Rectifier Considering Power Fluctuation. *Trans. China Electrotech. Soc.* **2021**, *36*, 305–319.
13. Wang, J.; Liu, S.; Zhang, Q. An Improved Control Method to Eliminate the Current Zero-Crossing Distortion for Vienna Rectifier. *Trans. China Electrotech. Soc.* **2022**, *37*, 3834–3844.
14. Song, W.; Huang, J.; Zhong, Y. A Hysteresis Current Control Method with Neutral Point Potential Balancing Control for Vienna Rectifier. *Power Syst. Technol.* **2013**, *37*, 1909–1914.
15. He, L.; Chen, X. Optimized PI Current Controller of Three Level Unidirectional PWM Rectifier Under Variable Inductance. *Trans. China Electrotech. Soc.* **2011**, *26*, 203–209.
16. Wu, M.; Ma, H.; Wei, Q. Study of Fractional Order PI DC-DC Converter Based on Dual Closed-Loop Control. *J. Phys. Conf. Ser.* **2023**, *2483*, 012028. [CrossRef]
17. Alfaro, C.; Guzman, R. Dual-Loop Continuous Control Set Model-Predictive Control for a Three-Phase Unity Power Factor Rectifier. *IEEE Trans. Power Electron.* **2022**, *37*, 1447–1460.
18. Badar, M.; Ahmad, I.; Rehman, S.; Nazir, S.; Waqas, A. Hierarchical control of hybrid direct current microgrid with variable structure based sliding mode control and fuzzy energy management system. *J. Frankl. Inst.* **2022**, *359*, 6856–6892. [CrossRef]
19. Ahmed, H.; Çelik, D. Sliding mode based adaptive linear neuron proportional resonant control of Vienna rectifier for performance improvement of electric vehicle charging system. *J. Power Sources* **2022**, *542*, 231788. [CrossRef]
20. Ma, H.; Xie, Y. A Novel Dual closed-Loop Control Strategy Based on Sliding-Mode Variable Structure of Vienna-Type Rectifier. *Trans. China Electrotech. Soc.* **2015**, *30*, 143–151.
21. Silva, J. Sliding-mode control of boost-type unity-power-factor PWM rectifiers. *IEEE Trans. Ind. Electron.* **1999**, *46*, 594–603. [CrossRef]
22. Wang, Y.; Li, Y.; Huang, S. An Improved Sliding Mode Direct Power Control Strategy Based on Reactive Power Compensation for Vienna Rectifier. *IEEE Access* **2022**, *10*, 15469–15477. [CrossRef]
23. Ma, H.; Yan, S.; Wang, S. Sliding-Mode Proportional Resonant Control of Three-Phase Vienna Rectifier. *Proc. CSU-EPSA* **2019**, *31*, 122–127+145.
24. Yang, X.; Chen, Y.; Jia, W. Vienna rectifier with voltage outer loop sliding mode control based on an RBF neural network. *Power Syst. Prot. Control* **2022**, *50*, 103–115.
25. Lv, K.; Wen, C.; Zhao, Q. Sensorless Control of Permanent Magnet Linear Synchronous Motor Based on Double Sliding Mode. *Recent Adv. Electr. Electron. Eng.* **2022**. [CrossRef]
26. Gao, P.; Pan, H. Model-free double fractional-order integral sliding mode control for permanent magnet synchronous motor based electric mopeds drive system. *IEICE Electron. Express* **2023**, *20*, 20230178. [CrossRef]
27. Wang, H.; Nie, J.; Li, B. Voltage Stability Control of Interface Converter in Hybrid Microgrid Based on Fractional-order Sliding Mode. *Proc. CSU-EPSA* **2024**, *36*, 141–149.
28. Zhu, Y.; Xia, L.; Zhang, Y. Second-Order Nonsingular Terminal Sliding Mode Model Predictive Control for Three-Phase Vienna Rectifier. *South. Power Syst. Technol.* **2024**, 1–9. Available online: http://kns.cnki.net/kcms/detail/44.1643.TK.20240730.1235.007.html (accessed on 22 October 2024).
29. Wang, T.; Li, X.; Zhang, J.; Chen, S.; Ma, J.; Lin, C. Fractional Sliding Mode Observer Control Strategy for Three-Phase PWM Rectifier. *World Electr. Veh. J.* **2024**, *15*, 316. [CrossRef]
30. Wang, T.; Zhang, J.; Li, X.; Chen, S.; Ma, J.; Han, H. The Control Strategies for Charging and Discharging of Electric Vehicles in the Vehicle–Grid Interaction Modes. *World Electr. Veh. J.* **2024**, *15*, 468. [CrossRef]